Robotica: (2020) volume 38, pp. 317–336. © Cambridge University Press 2019
doi:10.1017/S0263574719000614

# Snap-fit Assembly Process with Industrial Robot Including Force Feedback

László Rónai* and Tamás Szabó

*Robert Bosch Department of Mechatronics, University of Miskolc, Hungary.*
*E-mail: szabo.tamas@uni-miskolc.hu*

(Accepted April 1, 2019. First published online: May 14, 2019)

**SUMMARY**
This paper investigates a battery snap-in operation performed by an industrial robot. The snap-fit phenomenon is experienced during the insertion of batteries into the battery holder. In order to understand the nature of the snap-fit phenomenon, the large displacement but small deformation theory is used to model the insertion operation. The stability of equilibrium points is analysed in order to determine the so-called trip point. The purpose of the investigation is to augment the displacement control of the robot with force feedback. A microcontroller-based measurement system is implemented to provide the force feedback. The proposed method is valid for a class of snap-fit problems not only for the investigated specific one.

KEYWORDS: Snap-fit; Mechanical stability; Force feedback; Robot; Assembly.

## 1. Introduction

Snap-fit joints[1,2] are frequently used in engineering practice to join two different components.[3] During snap-in, one part is deflected and then locked into a depression on the joining partner.[4] When the joining operation is performed by a robot in ref. [5], the machine haptic concept should be utilized,[6–8] that is, the measurement of the force of the end effector is necessary. Determination of the load-deflection curve is essential. A great many papers analyse load deflection curves in case of snap through buckling phenomenon, for example, in refs. [9, 10] by models and experiments. The hysteresis curve in ref. [4] can be recorded during the snap-in and snap-out processes.

To treat the deflection of the investigated battery holder, large displacement theory of the beam model is required. The corotational approach[11,12] is often used for flexible structures to handle large rotations of finite elements. Determination of the stability of the equilibrium points is necessary to find the trip point, that is, the border of the stability. Mechanical stability in presence of non-conservative forces usually is analysed by the theorem proposed by Salvadori in ref. [13]. The results of the theoretical stability analysis can also be checked by simulation. The main purpose of this paper is to simulate the snap-fit process and determine the stability of the equilibrium points via measurement of the forces during insertion, where the end effector can release the battery. Thus, the snap-in operation is terminated automatically. Otherwise, due to displacement control, undesired high forces may occur or the battery may get stuck unexpectedly.

The rest of the paper is organized as follows: the corotational approach of the snap-fit process and the stability of the equilibrium points are described in Section 2. The equilibrium points of the snap-fit operation are also investigated by numerical simulation. Section 3 contains the displacement control of the industrial robot including force feedback. A commercial load cell and an amplifier unit are used to measure forces during insertion. The opening condition of the end effector is transmitted to the industrial robot by an AVR-type RISC (Reduced Instruction Set Computing)-based microcontroller. Practical measurements are performed to verify the snap-in and snap-out processes in Section 4.

* Corresponding author. E-mail: ronai.laszlo@uni-miskolc.hu


Fig. 1. The sequence of the batteries.

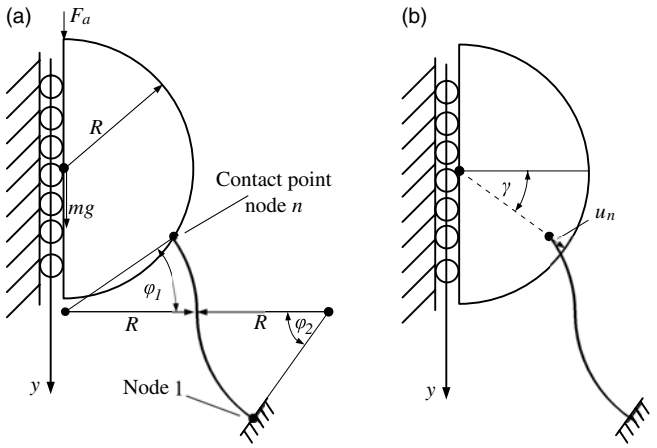


Fig. 2. (a) A 2D model of the battery and battery holder; (b) ensuring the kinematical contact condition.

Finally Section 5 has concluding remarks. Appendix contains a nomenclature of the scalar and matrix variables given in Tables AI and AII, respectively.

## 2. Modelling and Simulation of the Snap-fit Operation

A battery holder and one battery are shown in Fig. 1. In the sequel, snap-in and snap-out processes of one battery and the plastic holder will be modelled and simulated. The model of the snap-in operation is shown in Fig. 2 (a). Due to symmetry only half of the structure is considered with a two-dimensional (2D) model. The battery shown by a half circle is considered to be rigid. The radius $R$ of the battery is 9 mm. The battery holder is represented by a slender flexible curved beam. The curved beam consists of two arches having subtenses $\varphi_1$ and $\varphi_2$ with the same radius $R$ as the battery has. It is assumed that the rigid body and the flexible beam are in contact only in one point all along the snap-in and snap-out processes. The insertion of the battery in direction $y$ is prescribed by applying specified uniform displacement. The necessary assembly force to perform the snap-fit process is denoted by $F_a$.

In order to satisfy the kinematical contact condition (see Fig. 2 (b)), normal displacement $u_n$ has to be applied to the tip of the curved beam.

In the following, first the contact forces are determined for the snap-in and snap-out processes. Next the stability of the interested equilibrium points is analysed with the help of Salvadori's theorem. Then results of the theoretical stability analysis are checked by numerical simulation.

### *2.1. Modelling snap-in and snap-out processes*

The curved beam shown in Fig. 2 (a) is discretized by 2D straight beam elements without shear deformation with large displacements using corotational approach.[11] The number of elements $n_e$ is 20, the number of nodes $n$ is 21 and nodal point $n$ is the contact point. The initial and current

https://doi.org/10.1017/S0263574719000614 Published online by Cambridge University Press

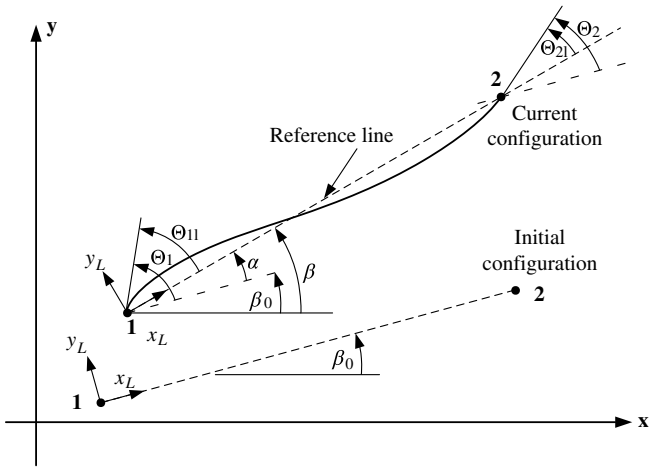


Fig. 3. The initial and current configurations of a beam element.

configuration of a beam element are shown in Fig. 3. Though the displacements and rotations are large, small strains are assumed.

The angle $\alpha$ is measured from the initial configuration; the nodal rotations $\Theta_1$, $\Theta_2$ are in the global coordinate system and the nodal rotations $\Theta_{1l}$, $\Theta_{2l}$ are in a local coordinate system; and the angle $\beta_0$ is the angle of the initial configuration and the angle $\beta$ gives the deformed configuration. According to Souza in ref. [14], the local nodal rotations can be determined without limitation on the range of the rotation of the element

$$\Theta_{1l} = \arctan\left(\frac{\cos\beta\sin\beta_1 - \sin\beta\cos\beta_1}{\cos\beta\cos\beta_1 + \sin\beta\sin\beta_1}\right) = \arctan\left(\frac{\sin\Theta_{1l}}{\cos\Theta_{1l}}\right), \tag{1}$$

$$\Theta_{2l} = \arctan\left(\frac{\cos\beta\sin\beta_2 - \sin\beta\cos\beta_2}{\cos\beta\cos\beta_2 + \sin\beta\sin\beta_2}\right) = \arctan\left(\frac{\sin\Theta_{2l}}{\cos\Theta_{2l}}\right), \tag{2}$$

where $\beta_1 = \Theta_1 + \beta_0$ and $\beta_2 = \Theta_2 + \beta_0$. The local axial displacement is calculated as proposed by Crisfield in ref. [11]:

$$u_L = \frac{L^2 - L_0^2}{L + L_0}, \tag{3}$$

where $L_0$ and $L$ are the lengths of the undeformed and the deformed beam elements, respectively.

The axial force in the beam is

$$P = \frac{EAu_L}{L_0}, \tag{4}$$

where $E$ is Young's modulus and $A$ is the area of cross section of the beam. The local end moments of the beam are related to the local nodal rotations

$$M_1 = \frac{EI}{L_0}(4\Theta_{1l} + 2\Theta_{2l}), \tag{5}$$

$$M_2 = \frac{EI}{L_0}(2\Theta_{1l} + 4\Theta_{2l}), \tag{6}$$

where $I$ is the area moment of inertia of the beam.

Assuming no forces are applied between the nodes of a beam element, the shear forces at the nodes are obtained as

https://doi.org/10.1017/S0263574719000614 Published online by Cambridge University Press

$$V_1 = \frac{M_1 + M_2}{L_0}, \tag{7}$$

$$V_2 = -\frac{M_1 + M_2}{L_0}. \tag{8}$$

The generalized nodal forces in Eqs. (4)–(8) are collected in the local internal element load vector $\bar{\mathbf{f}}_\mathbf{i}^\mathbf{e}$; see the Appendix. The corresponding vector of elementary nodal displacements $\bar{\mathbf{q}}^\mathbf{e}$ is also given in the Appendix. The element local internal load vector and the elementary nodal displacement vector are transformed in the same way to the global coordinate system ($x$, $y$):

$$\mathbf{f}_\mathbf{i}^\mathbf{e} = \mathbf{T}_\mathbf{e}^\mathbf{T} \bar{\mathbf{f}}_\mathbf{i}^\mathbf{e}, \qquad \mathbf{q}^\mathbf{e} = \mathbf{T}_\mathbf{e}^\mathbf{T} \bar{\mathbf{q}}^\mathbf{e}, \tag{9}$$

where $\mathbf{T}_\mathbf{e}^\mathbf{T}$ is the transpose of the transformation matrix $\mathbf{T_e}$ given in the Appendix. The structural internal load vector $\mathbf{f_i}$,

$$\mathbf{f_i} = \sum_e \mathbf{f}_\mathbf{i}^\mathbf{e}, \tag{10}$$

is obtained by performing the summation of all element vectors $\mathbf{f}_\mathbf{i}^\mathbf{e}$, which are of the same order as the internal load vector $\mathbf{f_i}$. All entries in $\mathbf{f}_\mathbf{i}^\mathbf{e}$ are zero except those which correspond to element $e$.[15]

Tangent stiffness matrix $\bar{\mathbf{K}}_\mathbf{t}^\mathbf{e}$ in local coordinate system was derived by Crisfield in ref. [11] via determining the changes in local 'strain producing' displacements and using virtual works both in local and the global coordinate systems. The local tangent stiffness matrix $\bar{\mathbf{K}}_\mathbf{t}^\mathbf{e}$ includes the local linear $\bar{\mathbf{K}}_\mathbf{L}^\mathbf{e}$ and geometric stiffness matrices $\bar{\mathbf{K}}_\mathbf{t1}^\mathbf{e}$, $\bar{\mathbf{K}}_\mathbf{t2}^\mathbf{e}$

$$\bar{\mathbf{K}}_\mathbf{t}^\mathbf{e} = \bar{\mathbf{K}}_\mathbf{L}^\mathbf{e} + \bar{\mathbf{K}}_\mathbf{t1}^\mathbf{e} + \bar{\mathbf{K}}_\mathbf{t2}^\mathbf{e}, \tag{11}$$

which are given in the Appendix. The element local stiffness matrix is also transformed to the global coordinate system ($x$, $y$):

$$\mathbf{K}_\mathbf{t}^\mathbf{e} = \mathbf{T}_\mathbf{e}^\mathbf{T} \bar{\mathbf{K}}_\mathbf{t}^\mathbf{e} \mathbf{T_e}. \tag{12}$$

The tangent stiffness matrix of the complete element assemblage is

$$\mathbf{K_t} = \sum_e \mathbf{K}_\mathbf{t}^\mathbf{e}, \tag{13}$$

where the summation is performed as in Eq. (10).

During the snap-in or snap-out processes, there is a single point mechanical contact between the battery and the battery holder. To describe the contact, one should introduce the terms of gap $d$ and contact pressure $p_c$. When the two bodies are in contact, $p_c \geq 0$ and the gap $d = 0$, otherwise $p_c = 0$ and $d > 0$ in the non-contact case. In the example considered here, the previous case holds during the investigation. Therefore, it is enough to ensure the kinematical condition, that is, $d = 0$, as it is shown in Fig. 2 (b).

It is advantageous to transform the displacements of the contacting node to a local coordinate system with axes in the normal and the tangential directions. The normal and tangential unit vectors are denoted $\mathbf{e_n}$ and $\mathbf{e_t}$. A transformation matrix $\mathbf{T_n}$ can be constructed based on vectors $\mathbf{e_n}$, $\mathbf{e_t}$, according to Fig. 2 (b):

$$\mathbf{T_n} = \begin{bmatrix} \cos\gamma & \sin\gamma & 0 \\ -\sin\gamma & \cos\gamma & 0 \\ 0 & 0 & 1 \end{bmatrix}. \tag{14}$$

The tangent stiffness matrix and the vector of internal forces can be decomposed into submatrices separating them in accordance with the last node $n$ and the rest of the nodes $r$:

$$\mathbf{K_t} = \begin{bmatrix} \mathbf{K_{t(r,r)}} & \mathbf{K_{t(r,n)}} \\ \mathbf{K_{t(n,r)}} & \mathbf{K_{t(n,n)}} \end{bmatrix}, \qquad \mathbf{f_i} = \begin{bmatrix} \mathbf{f_{i(r)}} \\ \mathbf{f_{i(n)}} \end{bmatrix}. \tag{15}$$

https://doi.org/10.1017/S0263574719000614 Published online by Cambridge University Press

The structural transformation matrix is also given by submatrices

$$\mathbf{T} = \begin{bmatrix} \mathbf{I} & \mathbf{0} \\ \mathbf{0} & \mathbf{T_n} \end{bmatrix}, \tag{16}$$

where $\mathbf{I}$ is a unit matrix having the order as the matrix $\mathbf{K_{t(r,r)}}$.

In awareness of the transformation matrix $\mathbf{T}$ and the tangential stiffness matrix $\mathbf{K_t}$ and the internal load vector $\mathbf{f_i}$ can be transformed as

$$\hat{\mathbf{K}}_\mathbf{t} = \mathbf{T}^\mathbf{T}\mathbf{K_t}\mathbf{T}, \tag{17}$$

$$\hat{\mathbf{f}}_\mathbf{i} = \mathbf{T}^\mathbf{T}\mathbf{f_i}. \tag{18}$$

Displacement boundary conditions at the clamped end of the curved beam and the prescribed displacement $u_n$ in node $n$ need to be considered, which can be performed as given in refs. [11, 15]. To fulfil the contact conditions, the contact node of the beam is pushed by a kinematical load, which is represented by a column vector $\mathbf{f_u}$ making use of the calculated displacement $u_n$ in normal direction (see Fig. 2 (b)). The formula of the displacement is

$$u_n = R - \sqrt{(x_0 - x_n)^2 + (y_0 - y_n)^2}, \tag{19}$$

where $R$ is the radius of the battery, $x_0$, $y_0$ are the coordinates of the battery's centre, and $x_n$, $y_n$ are the current nodal coordinates of the tip of the slender beam.

The tangential friction force $F_c$ is obtained by the sliding Coulomb friction law

$$F_c = \mu N, \tag{20}$$

which is exerted on node $n$ in the tangential direction and associated with load vector $\mathbf{f_c}$. The equations used for Newton–Raphson iteration are for $k = 1, 2, 3, \ldots$,

$${}^{\mathbf{t+\Delta t}}\hat{\mathbf{K}}_\mathbf{t}^{(\mathbf{k})}\,\boldsymbol{\Delta}\mathbf{q}^{(\mathbf{k})} = {}^{\mathbf{t+\Delta t}}\mathbf{f}_\mathbf{u}^{(\mathbf{k})} - {}^{\mathbf{t+\Delta t}}\mathbf{f}_\mathbf{c}^{(\mathbf{k-1})} - {}^{\mathbf{t+\Delta t}}\hat{\mathbf{f}}_\mathbf{i}^{(\mathbf{k-1})}. \tag{21}$$

$${}^{\mathbf{t+\Delta t}}\mathbf{q}^{(\mathbf{k})} = {}^{\mathbf{t+\Delta t}}\mathbf{q}^{(\mathbf{k-1})} + \boldsymbol{\Delta}\mathbf{q}^{(\mathbf{k})}, \tag{22}$$

with initial conditions

$${}^{\mathbf{t+\Delta t}}\mathbf{q}^{(\mathbf{0})} = {}^{\mathbf{t}}\mathbf{q}, \qquad {}^{\mathbf{t+\Delta t}}\hat{\mathbf{K}}_\mathbf{t}^{(\mathbf{0})} = {}^{\mathbf{t}}\hat{\mathbf{K}}, \qquad {}^{\mathbf{t+\Delta t}}\mathbf{f}_\mathbf{c}^{(\mathbf{0})} = {}^{\mathbf{t}}\mathbf{f}_\mathbf{c}, \qquad {}^{\mathbf{t+\Delta t}}\hat{\mathbf{f}}_\mathbf{i}^{(\mathbf{0})} = {}^{\mathbf{t}}\hat{\mathbf{f}}_\mathbf{i}, \tag{23}$$

where $\boldsymbol{\Delta}\mathbf{q}^{(\mathbf{k})}$ is a vector of incremental nodal point displacements.

The iteration is terminated when the following condition is satisfied:

$$\frac{\left\| \boldsymbol{\Delta}\mathbf{q}^{(\mathbf{k})} \right\|}{\left\| {}^{\mathbf{t+\Delta t}}\mathbf{q}^{(\mathbf{k})} \right\|} \leq tol, \tag{24}$$

where *tol* is a displacement convergence tolerance.

Making use of force entries $\hat{f}_{nx}, \hat{f}_{ny}$ of the internal load vector $\hat{\mathbf{f}}_\mathbf{i}$, the vertical component of the normal contact load ${}^{t+\Delta t}N_y$ is obtained in every time step as

$${}^{t+\Delta t}N_y = -{}^{t+\Delta t}\hat{f}_{nx} \sin\gamma \cos\gamma + {}^{t+\Delta t}\hat{f}_{ny}(\sin\gamma)^2. \tag{25}$$

It is noted that ${}^{t+\Delta t}N_y$ is regarded to be positive when it supports the battery in upward direction and negative when it pushes the battery downward.

A special purpose program has been developed to simulate the complete cycle of the snap-in and snap-out operations. The applied vertical displacement of the battery is 10.05 mm, which is subdivided into ± 30 uniform increments.

The material of the battery cell holder is polycarbonate/acrylonitrile butadiene styrene (PC/ABS). The Young's modulus $E$ of the battery holder is 2.415 GPa, the area of the cross section $A$ is 18.25 mm$^2$, and the area moment of inertia $I$ is 1.52 mm$^4$. A friction coefficient $\mu = 0.15$ is applied. The mass of the half battery is $m = 0.0229$ kg, and gravity $g$ equal to 9.81 m/s$^2$. The mass of the curved beam is neglected.

https://doi.org/10.1017/S0263574719000614 Published online by Cambridge University Press

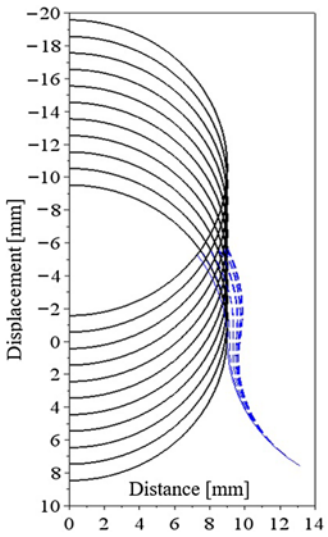


Fig. 4. The simulation process.

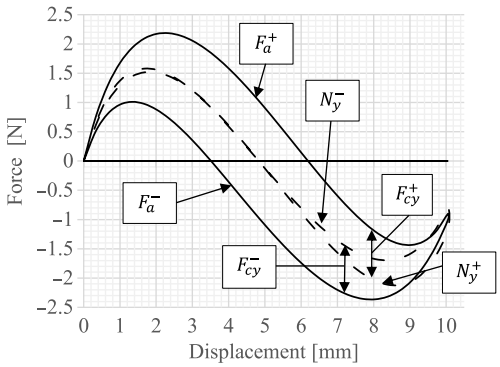


Fig. 5. Hysteresis of the insertion and removal operations.

The deformed shapes of the curved beam of the battery holder are drawn by dashed lines (see Fig. 4), noting that only every third step is displayed. The snap-in and snap-out forces are determined and shown in Fig. 5. Forces $F_{cy}^+$ and $F_{cy}^-$ are the vertical components of the Coulomb friction, and $N_y^+$ and $N_y^-$ are the vertical components of the normal forces computed for the snap-in and snap-out operations, respectively. The necessary snap-in force $F_a^+$ and snap-out force $F_a^-$ are denoted with solid lines. The dashed curved lines represent the vertical components of the normal supporting forces. The half weight of the battery is denoted by a horizontal dashed line. Figures 6 and 7 may help to interpret the meanings of $N_y^+$, $N_y^-$, $F_{cy}^+$ and $F_{cy}^-$. It is noted that $F_{cy}^+$ and $F_{cy}^-$ are positive value functions. The assembly forces $F_a^+$ and $F_a^-$ acting on the battery are obtained for downward and upward motions forming a loop or a hysteresis curve. A similar hysteresis curve was presented by Bader et al. in ref. [4] for snap-in and snap-out processes. The assembly forces are calculated as

$$F_a^+ = N_y^+ + F_{cy}^+, \tag{26}$$

$$F_a^- = N_y^- - F_{cy}^-. \tag{27}$$

The functions determined for the forces $N_y^+$, $N_y^-$, $F_{cy}^+$, $F_{cy}^-$, $F_a^+$ and $F_a^-$ can be used directly for the dynamic numerical analysis of the snap-in and snap-out processes in case of slip.

The values of the assembly forces $F_a^+$ and $F_a^-$ are different in any coordinate $y$. This fact gives an opportunity for occurring stick phenomenon when the motion of the battery is stopped and the direction of the velocity is changing while the assembly force is gradually changing from the

https://doi.org/10.1017/S0263574719000614 Published online by Cambridge University Press

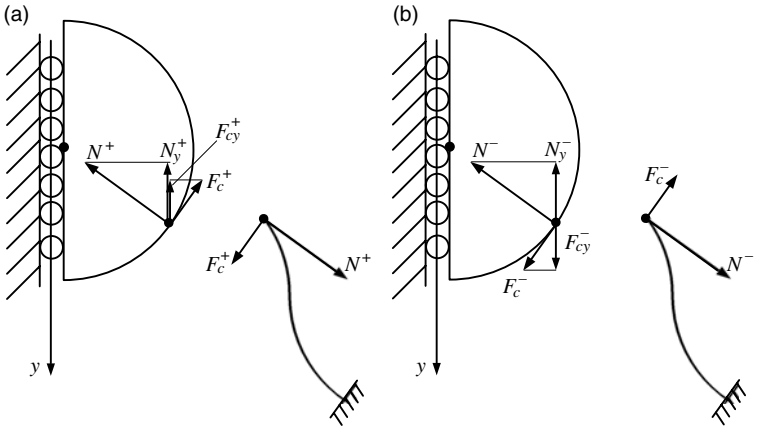


Fig. 6. Free body diagram in a slightly inserted position of the battery: (a) the velocity is positive; (b) the velocity is negative.

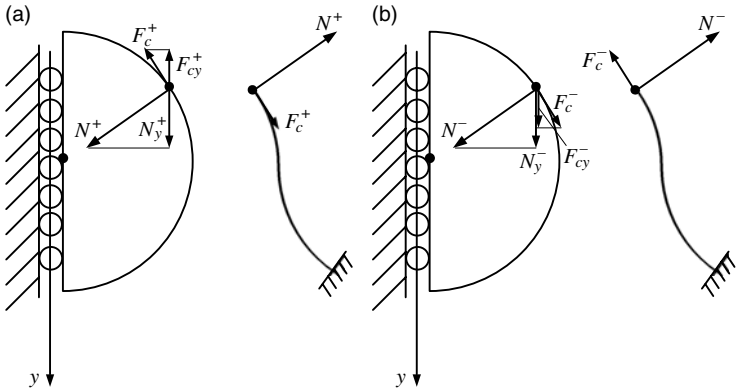


Fig. 7. Free body diagram in an almost inserted position of the battery: (a) the velocity is positive; (b) the velocity is negative.

value $F_a^+$ to $F_a^-$. It is assumed when only normal contact force is present, its vertical component is calculated as

$$N_y^{(0)} = \frac{F_a^+ + F_a^-}{2}, \tag{28}$$

where $N_y^{(0)}$ is also a function given in discrete points.

When adhesion takes place, that is, when stick may occur, a tangential force would also arise at the contact point in addition to the normal contact force. In order to determine the stiffness coefficient in vertical direction associated with the supporting curved beam, two additional computations are needed assuming frictionless contact, that is, $\mu = 0$. To perform it, first the vertical position of the node $n$ is determined due to contact. Then 1 N force is exerted on the deformed beam as shown in Fig. 8. The computed displacement increment $\Delta y$ provides the stiffness coefficient when the battery is at the location point $C$ (see Fig. 9):

$$k_y = \frac{1}{\Delta y} = \frac{1}{1.5643 \cdot 10^{-6}} = 6.393 \cdot 10^5 \text{ N/m}. \tag{29}$$

### *2.2. Stability of the equilibrium points*

The concept of stability was dealt with in mechanics to describe some types of equilibrium of a system in the early times.[13] Mechanical stability problems to be considered include dissipative friction forces in addition to conservative ones. Therefore, the stability of the equilibrium points could be analysed by Theorem 1, which is given as follows.

https://doi.org/10.1017/S0263574719000614 Published online by Cambridge University Press

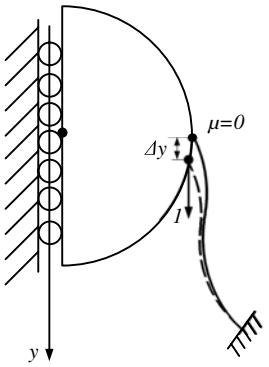


Fig. 8. Determination the stiffness coefficient $k_y$ in case of adhesion.

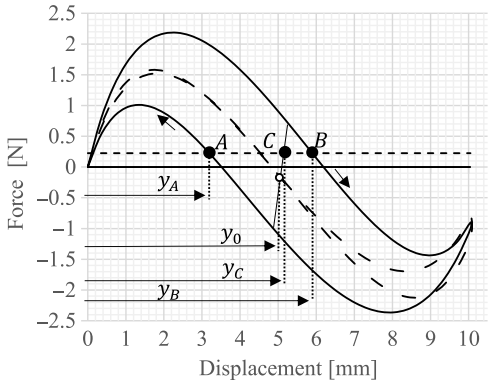


Fig. 9. Determination of the equilibrium points $A$, $B$ and $C$.

**Theorem 1.** (Salvadori in ref. [13]). *If the potential energy* $\Pi$ *has a minimum at* $\mathbf{q} = \mathbf{0}$*, the equilibrium at* $\mathbf{q} = \mathbf{0}$ *is isolated; the dissipation is complete, that is, for some function* $a \in \mathcal{K}$ *:* $(\mathbf{Q} \cdot \dot{\mathbf{q}}) \leq -a(\|\dot{\mathbf{q}}\|)$*, then the equilibrium* $\mathbf{q} = \dot{\mathbf{q}} = \mathbf{0}$ *is asymptotically stable. If* $\Pi$ *has no minimum at* $\mathbf{q} = \mathbf{0}$*, then the equilibrium* $\mathbf{q} = \dot{\mathbf{q}} = \mathbf{0}$ *is unstable.*

Remark: A function of class $\mathcal{K}$ is a function $a$: $\mathcal{R}^+ \to \mathcal{R}^+$, continuous, strictly increasing, with $a(0) = 0$. In Theorem 1, $\mathbf{q}$ is column vector of generalized displacements, $\dot{\mathbf{q}}$ is column vector of the generalized velocities and $\mathbf{Q}$ is row vector of the generalized forces.

The Voigt–Kelvin viscoelastic model is used to describe the adhesion, while sliding friction is given by the Coulomb law in ref. [16]. The friction force $F_{fy}$ in direction $y$ is given as

$$F_{fy} = \begin{cases} -F_{cy}^{+} sgn(\dot{y}), & \text{in case of slip, } \dot{y} > 0, \\ -F_{cy}^{-} sgn(\dot{y}), & \text{in case of slip, } \dot{y} < 0 \\ -k_y\,(y - y_0) - d_y \dot{y}, & \text{in case of stick,} \end{cases} \tag{30}$$

where $k_y$ is the stiffness coefficient and $d_y$ is the damping parameter, both of them being represented in direction $y$. Stick takes place if $F_a^-(y) < \left(N_y^0(y) + k_y\,(y - y_0)\right) < F_a^+(y)$.

Stability analysis of the equilibrium positions for $y \in [y_A; y_B]$ is performed in three equilibrium points $A$, $B$ and $C$ (see Fig. 9). Positions of points $A$, $B$ and $C$ are given as $y_A = 3.15$ mm, $y_B = 5.95$ mm and $y_C = 5.2$ mm, respectively. Slip takes place in the equilibrium points $A$ and $B$, while point $C$ is a candidate for stick. For the latter case in the vicinity of point $C$, the force displacement function is represented by a steep curve which is denoted by a thin solid line (see Fig. 9).

Equilibrium of point $A$ is written as (see Fig. 6 (b))

$$0 = mg - N_y^-(y_A) + F_{cy}^-(y_A). \tag{31}$$

https://doi.org/10.1017/S0263574719000614 Published online by Cambridge University Press

The potential energy associated with conservative forces is

$$\Pi(y) = -mgy + \int_0^y N_y^-(s)ds. \tag{32}$$

The derivative of Eq. (32) with respect to $y$ is

$$\left.\frac{\partial \Pi}{\partial y}\right|_{y_A} = -mg + N_y^-(y_A) \neq 0. \tag{33}$$

Comparing Eqs. (31) and (33), one can say that the potential energy has no minimum at the equilibrium point. Therefore according to Theorem 1, point $A$ is unstable. It means that the battery would be snapped-out unexpectedly.

The equilibrium equation in point $B$ is (see Fig. 7 (a))

$$0 = mg - N_y^+(y_B) - F_{cy}^+(y_B). \tag{34}$$

The potential energy of the conservative forces is

$$\Pi(y) = -mgy + \int_0^y N_y^+(s)ds. \tag{35}$$

The first derivative of Eq. (35) with respect to $y$ is

$$\left.\frac{\partial \Pi}{\partial y}\right|_{y_B} = -mg + N_y^+(y_B) \neq 0. \tag{36}$$

One can say that point $B$ is also unstable since the right-hand sides of Eqs. (34) and (36) are different. It means that point $B$ is a trip point; that is, the battery will snap-in autonomously.

The equilibrium of the intermediate point $C$ can be written according to Fig. 9 as

$$0 = mg - N_y^{(0)}(y_C) - k_y(y_C - y_0). \tag{37}$$

The coordinate $y_0$ represents the zero tangent contact force due to stick and is calculated as

$$y_0 = y_C - \frac{mg - N_y^{(0)}(y_C)}{k_y}, \tag{38}$$

and the obtained value of $y_0$ is 5.1992 mm. The $\Pi(y)$ potential in the vicinity of point $C$ is

$$\Pi(y) = -mgy + \int_0^y N_y^{(0)}(s)ds + \frac{1}{2}k_y\,(y - y_0)^2\,. \tag{39}$$

If the total potential energy has a minimum according to Theorem 1, the equilibrium point is stable. The first derivative of the potential energy is

$$\left.\frac{\partial \Pi}{\partial y}\right|_{y_C} = -mg + N_y^{(0)}(y_C) + k_y\,(y_C - y_0) = 0. \tag{40}$$

Comparing Eqs. (37) with (40), one can say that the potential energy may have a minimum, which can be confirmed by taking the second derivative of the potential energy with respect the displacement, that is,

$$\left.\frac{\partial^2 \Pi}{\partial y^2}\right|_{y_C} = \left.\frac{\partial N_y^{(0)}(y)}{\partial y}\right|_{y_C} + k_y > 0. \tag{41}$$

Since the value of $\left.\frac{\partial N_y^{(0)}(y)}{\partial y}\right|_{y_C}$ is $-696$ N/m, and the value of $k_y$ is $6.393 \cdot 10^5$ N/m, the total potential has a minimum at point $C$. Referring to Theorem 1 instead of column vectors, scalar variables are present in this example, that is, $\dot{q} = \dot{y}$ and $Q = -d_y\dot{y}$; furthermore, $-a(\|\dot{y}\|) = -\frac{1}{2}d_y\dot{y}^2$, point $C$ is asymptotically stable.

https://doi.org/10.1017/S0263574719000614 Published online by Cambridge University Press

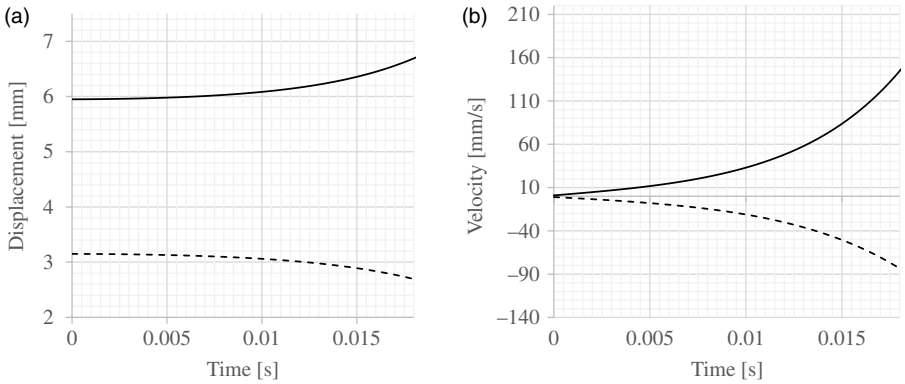


Fig. 10. (a) Displacements at points $A$ and $B$; (b) velocities at points $A$ and $B$.

*2.3. Numerical analysis of the equilibrium points A, B and C*

In this subsection, the stability results obtained in Section 2.2 will be checked by numerical simulation perturbing the equilibrium positions. Three initial value problems (IVPs) associated with equilibrium points $A$, $B$ and $C$ are set up.

IVP for point $A$ is

$$m\ddot{y} = mg - N_y^- + F_{cy}^-, \tag{42}$$

with initial values $y(0) = 3.15$ mm and $\dot{y}(0) = -1$ mm/s.

IVP for point $B$ is

$$m\ddot{y} = mg - N_y^+ - F_{cy}^+, \tag{43}$$

with initial values $y(0) = 5.95$ mm and $\dot{y}(0) = 1$ mm/s.

IVP for point $C$ is

$$m\ddot{y} = mg - N_y^0 - k_y\,(y - y_0) - d_y\dot{y}, \tag{44}$$

with initial values $y(0) = 5.2$ mm, $\dot{y}(0) = 1$ mm/s. The stiffness coefficient $k_y$ is $6.393 \cdot 10^5$ N/m and the damping parameter $d_y$ is $10^2$ Ns/m.

A special purpose program has been written to check the results of Section 2.2. Initial value problems for equilibrium points $A$, $B$ and $C$ have been solved numerically with time step $\Delta t = 10^{-6}$ s, and the obtained results for displacements and velocities are shown in Figs. 10 and 11. The displacements and velocities of the battery at point $A$ are denoted by dashed lines and the corresponding curves at point $B$ are represented by solid lines. The displacements and the velocities of the battery at the vicinity of point $A$ and point $B$ are increasing in time (see Fig. 10 (a) and (b)); therefore, these equilibrium points are unstable. The displacements and velocities of the battery at the vicinity of point $C$ are shown in Figure 11 (a) and (b). After velocity perturbation, the battery returns back to the equilibrium point $C$ . Thus point $C$ is asymptotically stable.

The numerical simulations confirm the results of the theoretical stability analysis based on Theorem 1.

## 3. Experimental Set-up and Control Strategy

The snap-in and snap-out processes are performed with a 6-DoF (Degrees of Freedom) Fanuc LR Mate 200iC industrial robot. A beam-type load cell is used to measure the assembly forces. The rated maximum measurable force of the load cell is 50 N – a holder unit has been designed and manufactured to fix it during the measurement (see Fig. 12). Furthermore, a supporting structure of the battery holder has been designed to keep the battery holder in a fixed position during assembly (see Fig. 13 (b)). The calculation of the necessary assembly force $F_a$ is based on the dimensions of Fig. 13 (a).

Tasks such as assembly, which involve extensive contact with the environment, are often better handled by controlling the forces of interaction between the manipulator and the environment rather than simply controlling the position of the end effector.[17]

https://doi.org/10.1017/S0263574719000614 Published online by Cambridge University Press

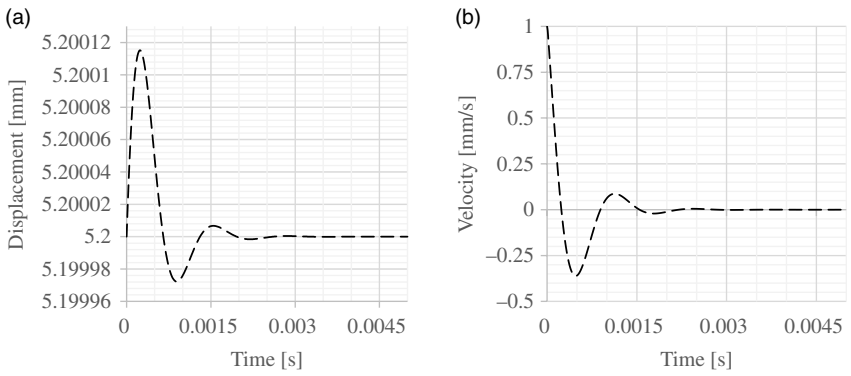


Fig. 11. (a) Displacements at point $C$; (b) velocities at point $C$.

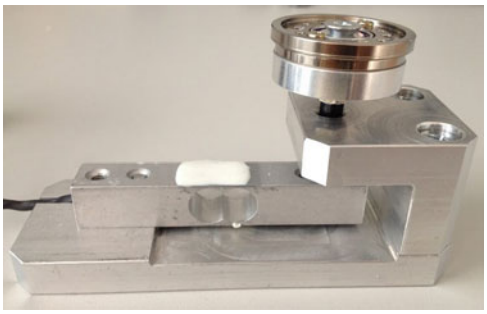

Fig. 12. The load cell.

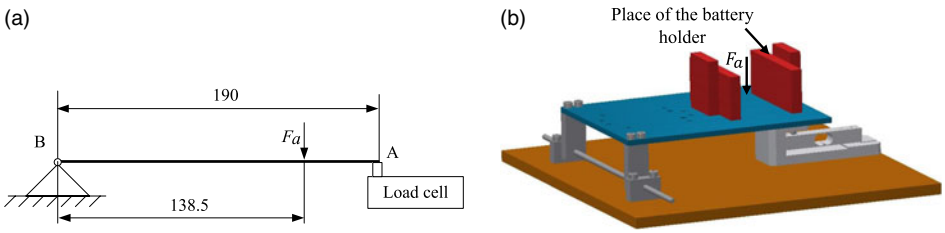


Fig. 13. (a) Dimensions of the supporting structure for the battery holder; (b) 3D model of the unit.

Since the function of the assembly force $F_a$ shown in Fig. 9 is not monotonic and double valued along the interested displacement region, force control is not applicable self-evidently. Choosing the weight of the battery as a reference value of the force feedback, it is equal to the assembly force in more than one point. It means that such a process would be prematurely terminated at the beginning of the assembly without reaching the trip point denoted by $B$. Force control could be applied on the curve section between the maximum value of the assembly force and the force at point $B$. However the maximum value of the assembly force is not known *a priori*, it can be predicted by simulation or measurement only approximately.

In addition to the difficulties mentioned above and the available Fanuc robot without open access controller, displacement control, that is, a set-point tracking control scheme, is used enhanced with force feedback for the sake of convenience. The force feedback is used for event handling, that is, to determine the location of the trip point. It is noted that the measured signal of the force feedback is converted into a Boolean variable, which is provided for the robot. Its reference value is Boolean *true*.

The block scheme of the test bench is shown in Fig. 14. An HX711 module is a 24-bit Sigma-delta A/D converter, which is specially designed for load cells. The module can produce up to 80 samples per second. The microcontroller ($\mu C$) is an AVR-type and RISC-based ATmega328, which can compute the values of the force. A printed circuit board was created to connect it with the A/D

https://doi.org/10.1017/S0263574719000614 Published online by Cambridge University Press

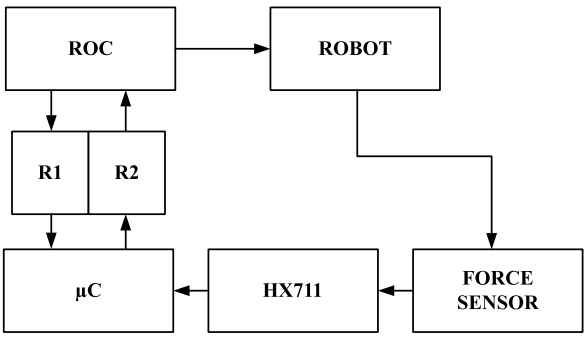


Fig. 14. The block scheme of the system.

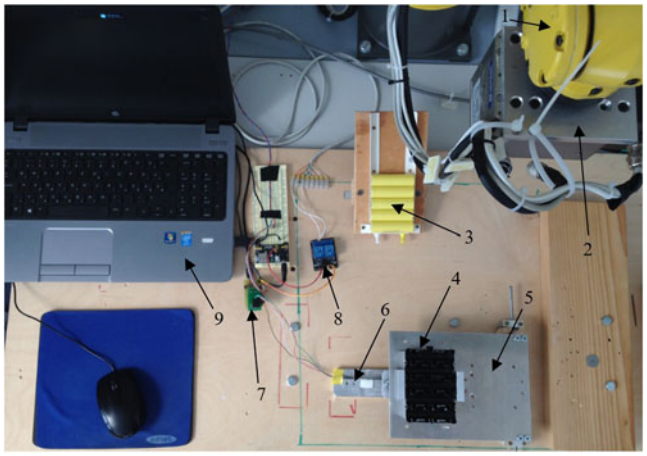


Fig. 15. The measurement system: 1 – Fanuc robot; 2 – end effector; 3 – battery; 4 – battery holder; 5 – supporting structure; 6 – load cell; 7 – $\mu$C and A/D converter; 8 – Relay $R2$; 9 – laptop.

converter module. The relays are represented by $R1$ and $R2$ (see Fig. 14). The $\mu C$ can send a signal to the R-30iA Mate robot controller (ROC), and vice versa by the relays.

The insertion of the battery based on displacement control enhanced with force feedback. In a step-by-step process, small increments in displacements are applied and the assembly force is checked in order to find the trip point in each increment. The test bench of the system, which can perform the assembling of batteries and battery holder, is shown in Fig. 15. The elements of the test bench are denoted by item numbers 1–9.

The robot moves from its base position to battery feeder (item 3) and grips the first battery. Thereafter, it is positioned close to the battery holder (item 4). The process continuous with calling a subroutine given in Table I. In which relay $R1$ is switched on for 0.1 s and then is switched off (see lines 1–3). Due to these commands, relay $R2$ is set to basic state. A target coordinate is defined and its initial value is equal to the assumed coordinate of the inserted battery (line 4). Thereafter the starting point of the insertion, that is, feed motion is above 10 mm from the assumed assembled position and then the robot is moved to this later position (see lines 5, 6). A cycle is defined between labels 1 and 2, in which displacement increments are applied step by step (see lines 8–11); furthermore the assembly force is measured by the $\mu C$. In each step, the displacement increment is equal to 0.5 mm. The end effector (item 2) is moved with constant velocity along these increments. The cycle is terminated when the trip point is reached given in line 10, which is based on the algorithm of the $\mu C$ given in Table II. The relay $R2$ of the $\mu C$ is represented by a digital input of the robot. Thereafter the battery is released by macro OPEN.

The algorithm given in Table II determines the trip point, which is located on the downhill side of the force displacement curve (see Fig. 5). It means that the peak of the curve should be passed during insertion. This peak value depends on also the velocity but it is usually roughly equal to a nominal force $F_{nom}$, which is determined by a previous experiment. The actual value of the assembly force is denoted by $F_{a,i}$ in step $i$ and its previous value is $F_{a,i-1}$. In order to find the maximum occurring force

https://doi.org/10.1017/S0263574719000614 Published online by Cambridge University Press

Table I. Subroutine to insert the battery

```
1     DO[107]=ON;
2     WAIT 0.1(sec);
3     DO[107]=OFF;
4     PR[79:TARGET]=PR[R[64]];
5     PR[79,3:TARGET]=PR[79,3:TARGET]+10;
6     J PR[79:TARGET] 100% FINE;
7     LBL[1];
8       PR[79,3:TARGET] = PR[79,3:TARGET]-DISPINCR;
9       J PR[79:TARGET] 100% CNT66;
10      IF DI[113] = ON,JMP LBL[2];
11      JMP LBL[1];
12    LBL[2];
13    OPEN;
```

Table II. Algorithm in order to find the trip point

```
1   if (F_{a,i} > F_max)
2     F_max = F_{a,i};
3   if((F_{a,i} < F_{a,i-1}) && (F_{a,i} < G_bat) && ((abs(F_max-F_nom)/F_nom) < ϵ))
4     {
5       Switch relay (R2);
6     }
```

a variable $F_{max}$ is used to store it (see lines 1–2), its initial value is equal to zero. The weight of the battery is denoted by $G_{bat}$. Passing the trip point the actual force is decreasing and smaller than $G_{bat}$. An additional condition, that is, the nominal force $F_{nom}$ and the maximum force $F_{max}$ are compared to each other when the difference is within a tolerant $\epsilon$, ensures that the trip point is not a premature one. The control flow diagram of the insertion process detailed above is also shown in Fig. 16.

To make a long story short, the displacement control of the robot is performed by the original R-30iA Mate Fanuc ROC using teach pendant programming technique, which provides digital input from the $\mu C$ determining the trip point. When the trip point is reached, the $\mu C$ sends a Boolean *true* signal to terminate the feed-motion of the robot and to open the end effector, otherwise it sends Boolean *false* signal.

## 4. Measurements

During the snap-in operation, the robot is controlled primarily by position. The force feedback augments the position control; that is, it interrupts in the trip point and lets the system terminate the snap-in process autonomously.

Measurements are performed to validate the results obtained by simulation. The hysteresis diagram of the assembling operation is shown in Fig. 17. The experimental measurement of the snap-in and snap-out operations are denoted by solid lines. The dashed lines represent the result of the simulation. The weight of one battery is indicated by dotted line. The points $A'$ and $B'$ are the trip points of the snap-in and snap-out operations, respectively. Between these points stick may take place.

During the snap-in operation point, $B'$ is unstable in accordance with Theorem 1. The insertion of the battery without force feedback is shown in Fig. 18 (a). One can see that the assembly force may reach undesirably high values. Displacement control including force feedback can resolve this problem because the end effector is opened at point $B'$ (see Fig. 18 (b)), and the snap-in process is terminated autonomously.

## 5. Conclusions

This paper presented a study about a battery snap-fit operation performed by an industrial robot. The main goal of the paper was to enhance the control of the robot by means of force feedback.

https://doi.org/10.1017/S0263574719000614 Published online by Cambridge University Press

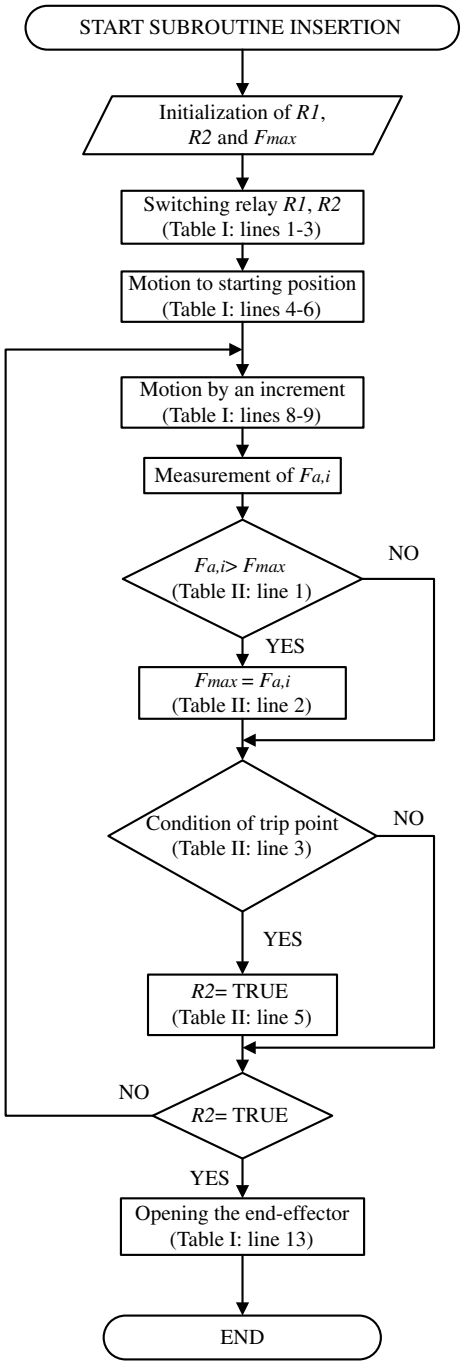


Fig. 16. Flow chart diagram of the snap-in process.

A flexible battery holder is modelled with a slender beam structure undergoing large displacements but small deformations using corotational approach. The simulation of the snap-in and snap-out processes provided the forces which were necessary to perform the operations. In awareness of the load history, what formed a hysteresis curve helped to determine equilibrium points including the trip point from which the snap-fit process was terminated autonomously. The equilibrium points have been studied analytically and numerically. The results obtained by analyses were verified by measurements. Experimental results and the computations showed a good agreement for the hysteresis curves. A test bench has been developed to measure the assembly forces and to evaluate the load history determining the trip point. The displacement control of a Fanuc robot was enhanced

https://doi.org/10.1017/S0263574719000614 Published online by Cambridge University Press

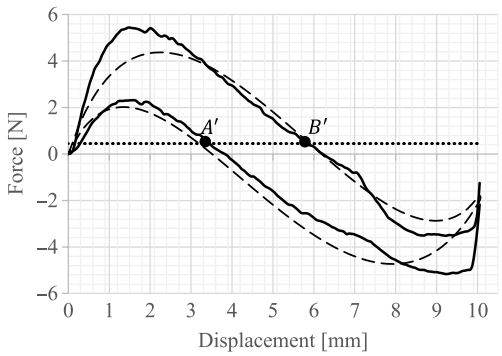


Fig. 17. Measurement of the insertion and removal operation.

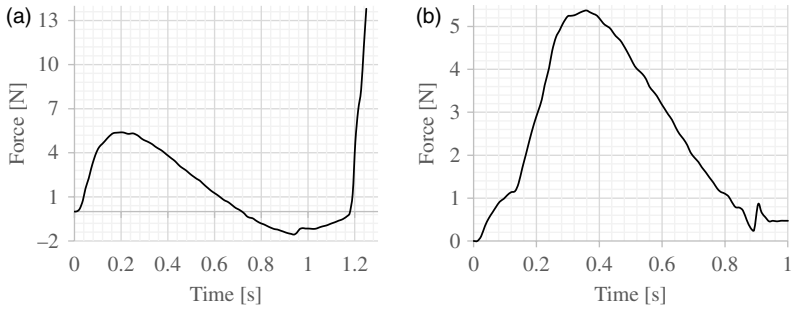


Fig. 18. Load history of the mounting operation: (a) without force feedback and (b) with force feedback.

with force feedback; at the trip point, the displacement control was interrupted and the end effector was opened. This technical solution can protect both the robot and the assembling structure from overloading.

The presented method can be used not only for battery snap-fitting, but also for a class of problems. For this reason, an intelligent end effector is planned to be designed, which can be applied for snap-fit operations in industrial circumstances.

## Acknowledgements

This study was supported by the ÚNKP-17-3 New National Excellence Program of the Ministry of Human Capacities. The authors would also like to thank Professor Emeritus István Páczelt for his constructive suggestions improving the clarity of the original manuscript.

## References

1. R. M. Kshirsagarl and D. B. Pawar, "Design and analysis of snap fit joint in plastic part," *Int. J. Innov. Emerg. Res. Eng.* **2**(1), 83–87 (2015).
2. C. Klahn, D. Singer and M. Meboldt, "Design Guidelines for Additive Manufactured Snap-Fit Joints," **In**: *Procedia CIRP 50*, vol. 75 (Elsevier, 2016) pp. 264–269.
3. Bayer MaterialScience LLC, "*Snap-Fit Joints for Plastics – A Design Guide*," (Bayer Polycarbonates Business Unit, Pittsburg, PA, 1998).
4. B. Bader and R. Koch, "Numerical simulation (FEM) of snap-in and snap-out processes of ball snap-fits," *Comput. Mater. Sci.* **3**, 125–134 (1994).
5. F. Pfeiffer, "Assembly processes with robotic systems," *Robot. Auton. Syst.* **19**, 151–166 (1996).
6. M. A. Srinivasan,"*What is Haptics. Laboratory for Human and Machine Haptics*," (Laboratory for Human and Machine Haptics: The Touch Lab, MIT, 2005) pp. 1–11.
7. B. S. Homberg, R. K. Katzschmann, M. R. Dogar and D. Rus, "Haptic Identification of Objects using a Modular Soft Robotic Gripper," **In**: *IROS* (2015) pp. 1698–1705.
8. V. J. Gohil, S. D. Bhagwat, A. P. Raut and P. R. Nirmal, "Robotics arm control using haptic technology," *Int. J. Latest Res. Sci. Technol.* **2**, 98–102 (2013).
9. J. Zhao, J. Jia, X. He and H. Wang, "Post-buckling and snap-through behavior of inclined slender beams," *J. Appl. Mech.* **75**, 041020-1–041020-7 (2008).

10. E. Riks, "An incremental approach to the solution of snapping and buckling problems," *Int. J. Solids Struct.* **15**(7), 529–551 (1979).
11. M. A. Crisfield, *Non-Linear Finite Element Analysis of Solids and Structures* (John Wiley and Sons, Chichester, UK, 1991).
12. M. Vahidi, V. Jafari, M. H. Abyaneh and S. H. Vahdani, "Displacement field approximations for force-based elements in large displacement analyses," *J. Appl. Math.* 1–11, (2012).
13. N. Rouche, P. Habets and M. Laloy, *Stability Theory by Liapumovs Direct Method* (Springer-Verlag, New York, 1977).
14. R. M. de Souza, "Force-based finite element for large displacement inelastic analysis of frames," *[Dissertation]* (Department of Civil and Environmental Engineering, University of California, Berkeley, 2000).
15. K. J. Bathe, *Finite Element Procedures* (Prentice Hall, Upper Saddle River, NJ, 1996).
16. S. Andersson, A. Söderberg and S. Björklund, "Friction models for sliding dry, boundary and mixed lubricated contacts," *Tribol. Int.* 580–587 (2005).
17. M. W. Spong, S. Hutchinson and M. Vidyasagar, *Robot Modeling and Control*, (John Wiley and Sons Inc., USA, 2006).

## Appendix

The local internal element load vector with the generalized nodal forces and the corresponding elementary nodal displacement vector are as follows:

$$\bar{\mathbf{f}}_{\mathbf{i}}^{\mathbf{e}} = \begin{bmatrix} -P \\ V_1 \\ M_1 \\ P \\ V_2 \\ M_2 \end{bmatrix}, \qquad \bar{\mathbf{q}}^{\mathbf{e}} = \begin{bmatrix} u_1 \\ v_1 \\ \Theta_{1l} \\ u_2 \\ v_2 \\ \Theta_{2l} \end{bmatrix}. \tag{A1}$$

The transformation matrix is

$$\mathbf{T_e} = \begin{bmatrix} \cos\beta & \sin\beta & 0 & 0 & 0 & 0 \\ -\sin\beta & \cos\beta & 0 & 0 & 0 & 0 \\ 0 & 0 & 1 & 0 & 0 & 0 \\ 0 & 0 & 0 & \cos\beta & \sin\beta & 0 \\ 0 & 0 & 0 & -\sin\beta & \cos\beta & 0 \\ 0 & 0 & 0 & 0 & 0 & 1 \end{bmatrix}, \tag{A2}$$

where $\beta$ is the angle of the deformed configuration (see Fig. 3).

The local elementary linear stiffness matrix of Eq. (11) is given as

$$\bar{\mathbf{K}}_L^e = \begin{bmatrix} \frac{AE}{L_0} & 0 & 0 & -\frac{AE}{L_0} & 0 & 0 \\ 0 & \frac{12EI}{L_0^3} & \frac{6EI}{L_0^2} & 0 & -\frac{12EI}{L_0^3} & \frac{6EI}{L_0^2} \\ 0 & \frac{6EI}{L_0^2} & \frac{4EI}{L_0} & 0 & -\frac{6EI}{L_0^2} & \frac{2EI}{L_0} \\ -\frac{AE}{L_0} & 0 & 0 & \frac{AE}{L_0} & 0 & 0 \\ 0 & -\frac{12EI}{L_0^3} & -\frac{6EI}{L_0^2} & 0 & \frac{12EI}{L_0^3} & \frac{-6EI}{L_0^2} \\ 0 & \frac{6EI}{L_0^2} & \frac{2EI}{L_0} & 0 & -\frac{6EI}{L_0^2} & \frac{4EI}{L_0} \end{bmatrix}. \tag{A3}$$

https://doi.org/10.1017/S0263574719000614 Published online by Cambridge University Press

Table AI. Scalar variables.

| Notation | Meaning |
|---|---|
| $R$ | Radius of the battery |
| $\varphi_1, \varphi_2$ | Two arches of the curved beam |
| $F_a$ | Assembly force |
| $u_n$ | Normal displacement |
| $x, y$ | Global Cartesian coordinate system |
| $x_L, y_L$ | Local Cartesian coordinate system |
| $n_e$ | Number of elements |
| $n$ | Number of nodes |
| $\alpha$ | Rigid-body rotation angle of beam |
| $\Theta_1, \Theta_2$ | Rotation of node 1, node 2 |
| $\Theta_{1l}, \Theta_{2l}$ | Rotation of node 1, node 2 in local frame |
| $\beta_0$ | Initial orientation angle for beam element |
| $\beta$ | Final orientation angle for beam element |
| $L_0$ | Initial length of beam element |
| $L$ | Current length of beam element |
| $P$ | Axial force in beam |
| $E$ | Young's modulus |
| $A$ | Area of beam |
| $M_1, M_2$ | Local end moments of beam at node 1, node 2 |
| $I$ | Area moment of inertia |
| $V_1, V_2$ | Shear forces of node 1, node 2 |
| $d$ | Contact gap |
| $p_c$ | Contact pressure |
| $\gamma$ | Angular coordinate of contacting point measured from horizontal line |
| $x_0, y_0$ | Initial coordinates of the battery's centre |
| $x_n, y_n$ | Current nodal coordinates of contact node $n$ |
| $F_c$ | Tangential friction force of contact node |
| $\mu$ | Friction coefficient |
| $t$ | Time |
| $\Delta t$ | Time increment |
| $tol$ | Displacement convergence tolerance |
| $\hat{f}_{nx}, \hat{f}_{ny}$ | Force entries of internal load vector in contact node $n$ |
| ${}^{t+\Delta t}N_y$ | Normal contact load |
| $m$ | Mass of the half battery |
| $g$ | Gravity |
| $F_{cy}^+, F_{cy}^-$ | Vertical components of the Coulomb forces |
| $N_y^+, N_y^-$ | Vertical components of the normal forces |
| $F_a^+, F_a^-$ | Assembly forces |
| $N_y^{(0)}$ | Vertical component of the normal force when only normal contact force is present |
| $k_y$ | Stiffness coefficient in vertical direction |
| $\Delta y$ | Computed displacement increment |
| $\Pi$ | Potential energy |
| $\mathcal{K}$ | A function $a$: $\mathcal{R}^+ \to \mathcal{R}^+$, continuous and strictly increasing |
| $F_{fy}$ | Friction force in direction $y$ |
| $d_y$ | Damping parameter |
| $y_0$ | The position of the zero tangent contact force |
| $A, B, C$ | Equilibrium points |
| $y_A, y_B, y_C$ | Position of the equilibrium points |

https://doi.org/10.1017/S0263574719000614 Published online by Cambridge University Press

Table AII. Matrices.

| Notation | Meaning |
|---|---|
| $\bar{\mathbf{f}}_{\mathbf{i}}^{\mathbf{e}}$ | Local internal element load vector |
| $\bar{\mathbf{q}}^{\mathbf{e}}$ | Local vector of elementary nodal displacements |
| $\mathbf{f}_{\mathbf{i}}^{\mathbf{e}}$ | Global internal load vector |
| $\mathbf{q}^{\mathbf{e}}$ | Global elementary nodal displacement vector |
| $\mathbf{T}_{\mathbf{e}}^{\mathbf{T}}$ | Transpose of transformation matrix |
| $\mathbf{f}_{\mathbf{i}}$ | Structural internal load vector |
| $\bar{\mathbf{K}}_{\mathbf{t}}^{\mathbf{e}}$ | Local tangent stiffness matrix |
| $\bar{\mathbf{K}}_{\mathbf{L}}^{\mathbf{e}}$ | Local linear stiffness matrix |
| $\bar{\mathbf{K}}_{\mathbf{t1}}^{\mathbf{e}}$, $\bar{\mathbf{K}}_{\mathbf{t2}}^{\mathbf{e}}$ | Local geometric stiffness matrices |
| $\mathbf{K}_{\mathbf{t}}^{\mathbf{e}}$ | Element stiffness matrix in global coordinate system |
| $\mathbf{K}_{\mathbf{t}}$ | Tangent stiffness matrix of the complete element assemblage |
| $\mathbf{e}_{\mathbf{n}}$, $\mathbf{e}_{\mathbf{t}}$ | Normal and tangential unit vectors |
| $\mathbf{T}_{\mathbf{n}}$ | Transformation matrix |
| $\mathbf{T}$ | Transformation matrix |
| $\mathbf{I}$ | Unit matrix |
| $\hat{\mathbf{K}}_{\mathbf{t}}$ | Transformed tangential stiffness matrix |
| $\hat{\mathbf{f}}_{\mathbf{i}}$ | Transformed internal load vector |
| $\mathbf{f}_{\mathbf{u}}$ | Column vector of the kinematical load |
| $\mathbf{f}_{\mathbf{c}}$ | Column vector of nodal point forces associated with friction force $F_c$ |
| $\hat{\mathbf{f}}_{\mathbf{i}}$ | Transformed vector of internal loads |
| $\Delta\mathbf{q}^{(\mathbf{k})}$ | Vector of incremental nodal point $k$ displacements in iteration step |
| ${}^{\mathbf{t+\Delta t}}\mathbf{q}^{(\mathbf{k-1})}$ | Vector of nodal point displacements at time $t + \Delta t$ in iteration step $k - 1$ |
| ${}^{\mathbf{t+\Delta t}}\mathbf{q}^{(\mathbf{k})}$ | Vector of nodal point displacements at time $t + \Delta t$ in iteration step $k$ |
| ${}^{\mathbf{t+\Delta t}}\hat{\mathbf{K}}_{\mathbf{t}}^{(\mathbf{0})}$ | Transformed stiffness matrix at time $t + \Delta t$ in initial step |
| ${}^{\mathbf{t+\Delta t}}\hat{\mathbf{K}}_{\mathbf{t}}^{(\mathbf{k})}$ | Transformed stiffness matrix at time $t$ in iteration step $k$ |
| ${}^{\mathbf{t+\Delta t}}\mathbf{f}_{\mathbf{u}}^{(\mathbf{k})}$ | Column vector of the kinematical load at time $t + \Delta t$ in iteration step $k$ |
| ${}^{\mathbf{t+\Delta t}}\mathbf{f}_{\mathbf{c}}^{(\mathbf{k-1})}$ | Vector of nodal point forces associated with friction force at time $t + \Delta t$ in iteration step $k - 1$ |
| ${}^{\mathbf{t+\Delta t}}\hat{\mathbf{f}}_{\mathbf{i}}^{(\mathbf{k-1})}$ | Transformed vector of internal loads at time $t + \Delta t$ in iteration step $k - 1$ |
| ${}^{\mathbf{t}}\mathbf{q}$ | Convergent solution vector of nodal point displacements at time $t$ |
| ${}^{\mathbf{t}}\hat{\mathbf{K}}$ | Stiffness matrix calculated at convergence at time $t$ |
| ${}^{\mathbf{t}}\mathbf{f}_{\mathbf{c}}$ | Convergent vector of nodal point forces associated with friction force $F_c$ at time $t$ |
| ${}^{\mathbf{t}}\hat{\mathbf{f}}_{\mathbf{i}}$ | Convergent transformed vector of internal loads at time $t$ |
| $\mathbf{q}$ | Column vector of generalized displacement |
| $\dot{\mathbf{q}}$ | Column vector of generalized velocities |
| $\mathbf{Q}$ | Row vector of generalized forces |
| $\mathbf{K}_{\mathbf{t(n,n)}}$ | Submatrix of the tangent stiffness matrix associated with contact node $n$ |
| $\mathbf{K}_{\mathbf{t(r,r)}}$ | Submatrix of the tangent stiffness matrix associated with rest of the nodes |
| $\mathbf{K}_{\mathbf{t(r,n)}}$ | Submatrix of the tangent stiffness matrix associated with contact node $n$ and rest of the nodes |
| $\mathbf{f}_{\mathbf{i(n)}}$ | Subvector of internal forces associated with contact node $n$ |
| $\mathbf{f}_{\mathbf{i(r)}}$ | Subvector of internal forces associated with rest of the nodes |

https://doi.org/10.1017/S0263574719000614 Published online by Cambridge University Press

The local geometric stiffness matrices are as follows:

$$\bar{\mathbf{K}}_{t1}^{e} = \begin{bmatrix} 0 & 0 & 0 & 0 & 0 & 0 \\ 0 & \frac{AEu_l}{L_0^2} & 0 & 0 & -\frac{AEu_l}{L_0^2} & 0 \\ 0 & 0 & 0 & 0 & 0 & 0 \\ 0 & 0 & 0 & 0 & 0 & 0 \\ 0 & -\frac{AEu_l}{L_0^2} & 0 & 0 & \frac{AEu_l}{L_0^2} & 0 \\ 0 & 0 & 0 & 0 & 0 & 0 \end{bmatrix}, \tag{A4}$$

$$\bar{\mathbf{K}}_{t2}^{e} = \begin{bmatrix} 0 & \frac{M_1+M_2}{L_0^2} & 0 & 0 & -\frac{M_1+M_2}{L_0^2} & 0 \\ \frac{M_1+M_2}{L_0^2} & 0 & 0 & -\frac{M_1+M_2}{L_0^2} & 0 & 0 \\ 0 & 0 & 0 & 0 & 0 & 0 \\ 0 & -\frac{M_1+M_2}{L_0^2} & 0 & 0 & \frac{M_1+M_2}{L_0^2} & 0 \\ -\frac{M_1+M_2}{L_0^2} & 0 & 0 & \frac{M_1+M_2}{L_0^2} & 0 & 0 \\ 0 & 0 & 0 & 0 & 0 & 0 \end{bmatrix}. \tag{A5}$$

The velocities and the accelerations are approximated by the Newmark method with trapezoid rule based on the following approximations:

$$^{t+\Delta t}y = {}^{t}y + \frac{\Delta t}{2}\left({}^{t}\dot{y} + {}^{t+\Delta t}\dot{y}\right), \tag{A6}$$

$$^{t+\Delta t}\dot{y} = {}^{t}\dot{y} + \frac{\Delta t}{2}\left({}^{t}\ddot{y} + {}^{t+\Delta t}\ddot{y}\right). \tag{A7}$$

The equations used in the Newton–Raphson iteration are given in the sequel for $k = 1, 2, 3, \ldots,$. The displacement is updated as

$$^{t+\Delta t}y^{(k)} = {}^{t+\Delta t}y^{(k-1)} + \Delta y^{(k)}. \tag{A8}$$

The velocity is calculated as

$$^{t+\Delta t}\dot{y}^{(k)} = \frac{2}{\Delta t}\left({}^{t+\Delta t}y^{(k-1)} + \Delta y^{(k)} - {}^{t}y\right) - {}^{t}\dot{y}. \tag{A9}$$

The acceleration is given as

$$^{t+\Delta t}\ddot{y}^{(k)} = \frac{4}{\Delta t^2}\left({}^{t+\Delta t}y^{(k-1)} + \Delta y^{(k)} - {}^{t}y\right) - \frac{4}{\Delta t}{}^{t}\dot{y} - {}^{t}\ddot{y}. \tag{A10}$$

IVP for point $A$ is

$$m\,{}^{t+\Delta t}\ddot{y}^{(k)} + (k_e + k_s)\,\Delta y^{(k)} = mg - {}^{t+\Delta t}N_y^{-(k-1)} + {}^{t+\Delta t}F_{cy}^{-(k-1)}, \tag{A11}$$

with initial values $^{t+\Delta t}y(t) = {}^{t}y$, $^{t+\Delta t}\dot{y}(t) = {}^{t}\dot{y}$ and $^{t+\Delta t}\ddot{y}(t) = {}^{t}\ddot{y}$,

where $k_e = \left.\frac{\partial N_y^-}{\partial y}\right|_{t+\Delta t y^{(k-1)}} = k_e$ and $k_s = \left.\frac{\partial F_{cy}^-}{\partial y}\right|_{t+\Delta t y^{(k-1)}}$.

IVP for point $B$ is

$$m\,{}^{t+\Delta t}\ddot{y}^{(k)} + (k_e - k_s)\,\Delta y^{(k)} = mg - {}^{t+\Delta t}N_y^{+(k-1)} - {}^{t+\Delta t}F_{cy}^{+(k-1)}, \tag{A12}$$

with initial values $^{t+\Delta t}y(t) = {}^{t}y$, $^{t+\Delta t}\dot{y}(t) = {}^{t}\dot{y}$ and $^{t+\Delta t}\ddot{y}(t) = {}^{t}\ddot{y}$,

https://doi.org/10.1017/S0263574719000614 Published online by Cambridge University Press

where $k_e = \left.\frac{\partial N_y^+}{\partial y}\right|_{t+\Delta t y^{(k-1)}} = k_e$ and $k_s = \left.\frac{\partial F_{cy}^+}{\partial y}\right|_{t+\Delta t y^{(k-1)}}$.

IVP for point $C$ is

$$m\,{}^{t+\Delta t}\ddot{y}^{(k)} + \left(k_e + k_y\right)\Delta y^{(k)} = mg - {}^{t+\Delta t}N_y^{0(k-1)} - k_y\left({}^{t+\Delta t}y^{(k-1)} - y_0\right) - d_y\,{}^{t+\Delta t}\dot{y}^{(k)}, \tag{A13}$$

with initial values ${}^{t+\Delta t}y(t) = {}^{t}y$, ${}^{t+\Delta t}\dot{y}(t) = {}^{t}\dot{y}$ and ${}^{t+\Delta t}\ddot{y}(t) = {}^{t}\ddot{y}$,

where $k_e = \left.\frac{\partial N_y^0}{\partial y}\right|_{t+\Delta t y^{(k-1)}} = k_e$ and $k_y = 6.393 \cdot 10^5 \frac{N}{m}$ and $d_y = 10^2\ \frac{Ns}{m}$.

Substituting (A9) and (A10) into (A11)–(A13) then performing straightforward manipulations, the unknown displacement increment $\Delta y^{(k)}$ can be determined for the three initial value problems defined above.

https://doi.org/10.1017/S0263574719000614 Published online by Cambridge University Press